Investigation of biochemical properties of flash sintered ZrO$_2$–SnO$_2$ nanofibers

Zeynep Çetinkaya [a,*], Eda Güneş [b], İlyas Şavkliyildiz [a]

[a] Department of Metallurgical and Materials Engineering, Konya Technical University, Konya, Turkey
[b] Department of Gastronomy and Culinary Arts, Necmettin Erbakan University, Konya, Turkey

HIGHLIGHTS

- The ternary system of ZrO$_2$–SnO$_2$–Zr-SnO$_4$ CNFs were produced by electrospinning technique.
- As the volume of SnO$_2$ increases in the CNFs, diameters of the fibers tend to decrease along with decrement in the band gap.
- The max power absorption of 1.58 W/mm^3 in flash sintering let to highly dense nanocompositions in less than 80secs.
- Sintered nanocompositions were revealed antimicrobial activity both on *E. coli* and *S. aureus*.
- No increases the toxicity (survival rate, development time and oxidative stress index) was observed in the model organism.

GRAPHICAL ABSTRACT
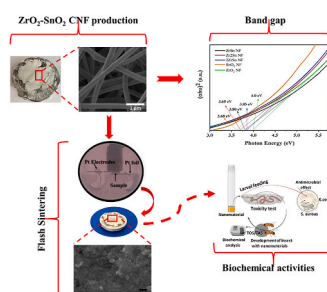
ABSTRACT

ZrO$_2$–SnO$_2$ nanocomposition were produced in nanofibers (NFs) form with three various mixing volume ratio by electrospinning technique. The microstructure and morphological characterization of NFs reveals the ternary system of ZrO$_2$–SnO$_2$–ZrSnO$_4$. Furthermore, Band gap structure of NFs was varied with the composition ratio which consequently affect the Flash sintering (FS) event. The FS experiments were utilized under thermal (844–878 °C) and electric field (420 V/mm) with 3.77 mA/mm^2 current cutoff. Highly dense nanocomposition were obtained in less than 80secs with a max power absorption of 1.58 W/mm^3. Thanks to low sintering temperature and time, nanostructured surface morphology were acquired which is crucial for biochemical properties of nanocompositions. *Drosophila melanogaster* food was covered with sintered nanocompositions and the control food. The toxicity of the nanomaterial in the insect, survival rate(%), development time(days) were investigated. In order to support the results, biochemical analyzes (total oxidative level-TOS, total antioxidant level-TAS and oxidative stress index-OSI) were performed in adults. In addition, antimicrobial activity was evaluated with *Escherichia coli* and *Staphylococcus aureus*. It was determined that the nanomaterials had an antimicrobial effect along with non-toxic effect on the insect. Besides, it did not change the survival rate of the insect in all groups. Although there was a one-day difference in development times, it did not cause a statistical change in the OSIs of female and male individuals. We believe that the synthesized nanocompositions can be used as a valid candidate

* Corresponding author.
  E-mail address: zcetinkaya@ktun.edu.tr (Z. Çetinkaya).

in the healthcare system, such as dental implants, due to its antimicrobial effect and non-toxicity in the model organism.

1. Introduction

Energy is one of the demands that people have in almost every aspect of their lives. As the world's population increases and the rate of consumption of resources increases, the choices people make regarding energy consumption become more significant [1].

As the world moves towards these global environmental problems more rapidly, researching ways to use energy resources more economically attracts great attention. In the last decade, energy saving has become a major trend in the world, leading people to use less energy. The biggest effects of energy saving are seen in industrial applications, which is one of the intensive use areas of energy. It is a known fact that the savings practices to be made in many different industry applications will greatly benefit companies and humanity, as well as their global effects. With all technologies that will save electricity, production costs will decrease, and nature pollution in countries that produce electricity from fossil fuels will be prevented to a large extent [2].

Sintering in ceramic materials means that the particles that come into contact with each other are bonded together at high temperatures, joining without melting [3,4]. This bonding is formed by atomic movements in the solid state below the melting temperature. In traditional ceramic densification, sintering involves long-term heat treatments at elevated temperature to acquire have highly dense material. The reduction of pores in the sintering process; The initial porosity ratio in the green compact material is determined by the sintering temperature and sintering time [3,4]. Many different methods are used for the sintering of ceramic materials. Some of those; non-pressure sintering, hot isostatic pressing (HIP) [5], gas pressure sintering (GPS) [6], spark plasma sintering (SPS) [7] and FS [8,9] methods. Among these methods, the most frequently used method for sintering zirconia in the literature is; fired with conventional sintering furnaces at 1350–1550 °C between 2 and 5 h [10]. Due to the high temperature and longtime used in sintering methods, the electricity consumption increases considerably.

The most basic example that can be given to the sintering process using electric current is SPS [7]. Although the sintering temperature cannot be reduced much with this method, the sintering time can be shortened considerably. In SPS, joule heating is applied to the ceramic material in the graphite mold with the principle of low voltage, very high current. The FS method using a DC electric field, in which the densification of materials takes place in a very short time and a relatively low temperature, has received great attention in recent years [9, 11,12]. In the FS method, the invention of which was made a short time ago, low voltage is applied to the ceramic sample prepared by powder pressing, in the furnace, and the furnace temperature is increased at a certain speed. Unlike SPS, the electric field is only applied to the sample and the applied voltage is kept at a low level. But then, depending on the type of conductivity (electronic, ionic or polaron) and the forbidden band gap (band gap, E_g), when the mass reaches a certain temperature, its conductivity increases spontaneously and electric current passes through the sample [13–17]. The electrical current passes over the sample for only 20–30 s and during this period, very rapid physical shrinkage/shrinkage occurs in the sample, and the sample density increases from 55% to 97% and above. FS methods is suitable for generally semiconductors [18]. Current leakage temperature, incubation time and on-set of FS are chiefly related with the thermal and electric field applied on sample along with the materials properties such as conductivity and band gap [19,20]. In addition, among all the sintering methods mentioned above, when the FS method is used, time and temperature, therefore energy can be saved considerably.

The transition metals of Zr, Hf, Mo, and Ti, which have high band gaps in the range of 3.0–7.0, are commonly used in various industries.

Among these, ZrO_2 exhibits exceptional mechanical and structural stability and has a high melting temperature (2715 °C). There are wide applications of ZrO_2 materials in various fields such as biomedical (for example, implant and artificial bone) and industrial applications [2, 21–23]. Although ZrO_2 has been known as an electrical substrate or an electrode material, it has rarely been considered as an actual electrical material due to its high band gap (above 5 eV). Due to its unique properties, it is considered a promising building block for nanocompositions. Its high hardness, thermal stability and chemical inertness make it an ideal choice for various applications.

The three crystal phases of SnO_2 are defined as tetragonal, cubic, and orthorhombic. The former has different chemical and physical properties than the latter. The orthorhombic phase is related to the synthesis method and various experimental conditions. SnO_2 is a type of semiconductor that exhibits oxygen-deficit properties. It can be used as a catalyst by doping with other elements. ZrO_2 is a commonly used transition metal that exhibits high chemical stability, low toxicity, and mechanical strength. In recent years, scientists have frequently studied the effect of secondary metal oxides added to metal oxides [24–26]. Due to the special surface acidity of ZrO_2 and the electrical properties of SnO_2, zirconium and tin oxides (ZrO_2 and SnO_2) are known examples of n-type semiconductor oxides and are widely used in many different applications in the literature such as gas sensors, solar cells, catalysts and optoelectronic devices considered as a subject.

Few articles have been studied in the literature on ($ZrSnO_4$) nanoparticles and thin films synthesized by various techniques such as sol-gel [27,28], hydrothermal method [29,30] and co-precipitation [31,32]. However, as far as we know and research in the literature, there is no article about the production of ZrO_2–SnO_2 nanocomposition materials as NFs and their FS.

In this study, ZrO_2–SnO_2 (n-n type) nanocomposition fibers produced in different ratios and the effect of composition ratio in FS were investigated. With this technique, it is also aimed to save energy by reducing the sintering temperature and time in the selected material systems, and to improve the mechanical properties of the final product by preventing grain growth. Moreover, the biocompatibility of ZrO_2–SnO_2 nanocomposition materials was investigated for its possible usage in bio applications. Depending on the way they are taken or contacted, metals and nanoparticles can cause oxidative stress in the cell and cell wall of living things, and biocompatible nanomaterials are preferred for their antioxidant activities [33–35]. Oxidative stress caused by free radicals is associated as one of the most important causes of toxicity. The toxic effects of nanoparticles are tested using various bioindicator model organisms such as bacteria and *Drosophila melanogaster* [36,37]. *D. melanogaster* Meigen used to study the toxicity elicited by various nanoparticles [38]. Among the model organisms, *D. melanogaster* is highly preferred for many reasons such as its similarity to humans, easy-cheap supply and cultivation, high probability of repetition, and not requiring ethics. Oxidative stress index (OSI = total oxidation level-TOS/total antioxidant level-TAS), which is an easy-to-understand, sensitive, automatic and inexpensive method, provides convenience in understanding the effectiveness of the substances used in the experiments. By using the antioxidant properties of metal oxide nanoparticles: The study was designed with the aim of understanding that the new material that can be used in treatments for not only absence of toxicity in the larval stage, but also scavenging of reactive oxygen species that can be produced between genders in the adult period.
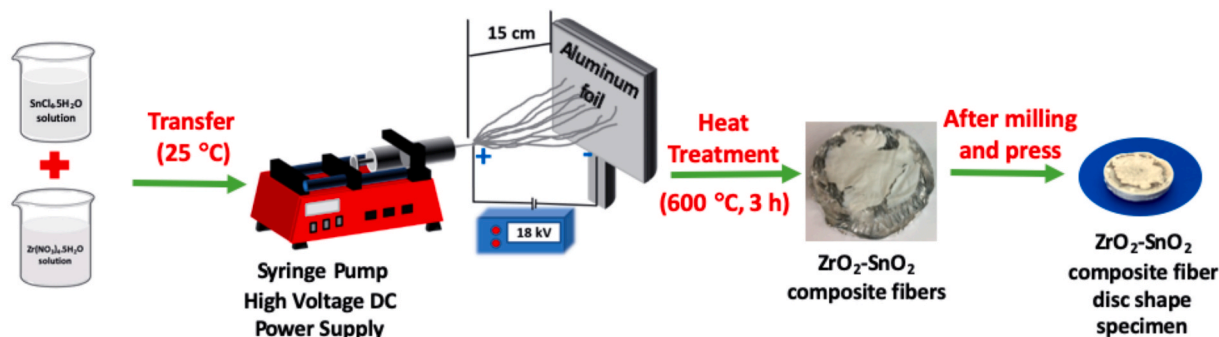
Fig. 1. Scheme of the preparation of ZrO$_2$–SnO$_2$ CNFs.

2. Experimental

2.1. Chemicals

Zirconium (IV) nitrate pentahydrate (Zr(NO$_3$)$_4$.5H$_2$O, China) and tin (IV) chloride pentahydrate (SnCl$_4$.5H$_2$O, Sigma Aldrich) was used as a precursor. Polyvinyl pyrrolidone (PVP, M$_w$ = 1.3 × 10^6, Sigma-Aldrich) was used as for the preparation of electrospinning solution. Acetic acid (Tekkim), ethanol (C$_2$H$_5$OH, %99 pure) and N–N-dimethyl formamide (DMF, %99 pure) were purchased from Sigma- Aldrich. All chemicals were used as received without any further purification.

2.2. Preparation of the ZrO$_2$–SnO$_2$–ZrSnO$_4$ ternary NFs (CNFs)

Zirconium (IV) nitrate pentahydrate and tin (IV) chloride pentahydrate were used as a precursor in conjunction with solvent additives such as ethanol, acetic acid and DMF. Electrospinning solution was prepared and CNFs were collected on electrically conductive Al foil substrate. Then, those composite NFs were heat-treated (calcination) in air to obtain ZrO$_2$–SnO$_2$–ZrSnO$_4$ CNFs. In the first step of the synthesis, 0.15 g PVP was dissolved in a solvent consisting of 2.5 ml ethanol and 1 ml acetic acid for 2 min at 50 °C. Then, 1.5 g Zr(NO$_3$)$_4$.5H$_2$O was added in the solution for 20 min at 50 °C and transparent solution was turned into white color. Before electrospinning process the solution was cooled to room temperature. Another solution for electrospinning was produced in a typically SnO$_2$ solution procedure. 1.2 g SnCl$_4$.5H$_2$O was dissolved in 6.6 ml DMF and 6.6 ml ethanol solution, for 1 h at 30 °C. Then, 1.2 g PVP was added into the solution and stirred for 16 h at 48 °C. At that temperature the color of the solution remained white. After cooling the room temperature the solution color turned into transparent [39]. To prepare ZrO$_2$–SnO$_2$–ZrSnO$_4$ CNFs, two different solution mixed (ZrO$_2$–SnO$_2$), (%v/v) in three different composition (ZrO$_2$–SnO$_2$ – ZrSn; 1/1, ZrO$_2$–2SnO2 –Zr2Sn; 1/2, 2ZrO$_2$–SnO$_2$ – 2ZrSn; 2/1). The solutions were prepared in the determined ratios and mixed for 30 min at room temperature for homogenization before the electrospinning process (Fig. 1).

For the electrospinning process, composite viscous precursor was transferred into the syringe with the 22 ½-gauge stainless steel needle. The tip was electrified using a high voltage DC-power supply (Spellman SL30) under an applied voltage of 18 kV. Distance between the tip of the needle and collector was set as 10 cm. The feeding rate of the solution was adjusted to 0.8 mL/h (Fig. 1). The collected CNFs were dried in ambient air overnight then calcined at 550 °C with a heating rate 3 °C/min and kept at this temperature for 5 h under atmospheric conditions to remove any organics [40].

2.3. Characterization

FT-IR spectra of the ZrO$_2$, SnO$_2$ and Zr–SnO$_2$ CNFs were recorded 4000-400 cm^{-1} using ATR method in PerkinElmer GX Spectrometer with a wave number resolution is 1 cm^{-1}. Phase identification of the NFs
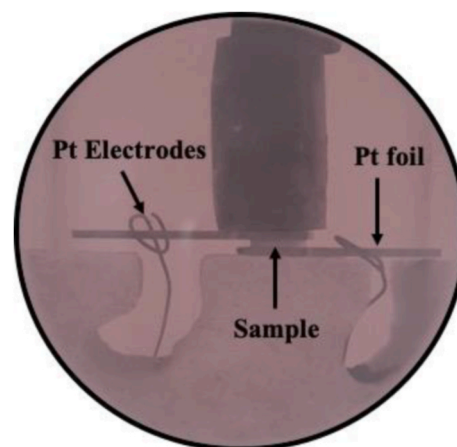

Fig. 2. Parallel plate capacitor geometry experimental setup conducted during FS [41–43,46,47].

is done by X-Ray diffraction (XRD, Bruker D8 Advance, Cu–K α, $\lambda = 1.54$ Å). The scanning speed was determined as 2°/min from 10 to 80°. Microstructural analysis of as-collected and annealed NFs was investigated by scanning electron microscopy (SEM, SM-Zeiss LS-10). The size and distribution of the ZrO$_2$–SnO$_2$–ZrSnO$_4$ composite NFs were calculated with the *Image J* software. UV–Vis spectra of the samples were determined by VWR 3100-PC UV–Vis spectrophotometer from 250 to 900 nm to examine the band gap properties.

2.4. Flash sintering sample preparations

The heat-treated ZrO$_2$–SnO$_2$–ZrSnO$_4$ CNFs were ball-milled for 1 h using zirconia (ZrO$_2$) grinding media. After this process, it is seen in Fig. S3 that the NFs are not deformed, but the length of the fibers is shortened. The milled powder was blended with 5 wt% polyethylene glycol (PEG, C$_2$H$_6$O$_2$) then, hardened stainless steel die was utilized for pressing powder into disc shape (13 mm diameter and 1.5 mm thickness) under 200 MPa [41–43]. The disc shape specimen is placed in a parallel plate capacitor experimental setup for electric field assisted experiment [44,45]. To applied electric field, the specimens' surface was covered with platinum foils, which allowed us to implement ohmic contacts. They were then attached to the wires of the power source. The variation in current and voltage values were monitored as a function of time instead of temperature. Because, the current leakage on the sample could have contributed to the extra temperature rise in the furnace due to the joule heating during FS operation. Fig. 2 shows the FS setup in the furnace [41–43,46,47]. Two wires to act as electrodes were placed above and below the samples ready for the experiment. Silver, copper, steel and platinum wires can be used in experiments to apply an electric field. In this study, both sides of the sample are covered with platinum

foils, which are used to apply the electric field and ensure a temporary current draw by the ZrO_2–SnO_2–$ZrSnO_4$ CNFs sample throughout the entire experimental cycle. Using platinum foil, homogeneous and uniform electric field and ohmic contact on the sample surface was applied to both sides of the sample. Insulated inlets have been prepared to allow the entry of the electrodes used to apply the electric field during FS into the furnace. Platinum foils are attached to the power supply located outside the furnace with stainless steel wires.

The furnace temperature is programmed to be increased up to 900 °C with a heating rate of 20 °C/min. The DC power supply was utilized to apply an electric field of 420 V/mm to the specimen during FS. The current cut-off value was chosen as 3.77 mA/mm^2 to prevent excessive joule heating. Voltage and current values are collected as a function of time instead of temperature. Because, the current draw thorough the specimen could have contributed to the extra temperature rise in the furnace due to the joule heating during Flash operation. With our knowledge, studies and literature researches so far, both electric field and current cut-off values have been determined. The microstructure on the sintered sample surface was investigated using a scanning electron microscope (SEM, SM Zeiss LS-10). X-ray diffraction spectrometry (Rigaku ZSX Primus-II XRD) was used for physical and chemical structure analysis within the UK.

2.5. Toxicity and biochemical tests

D. melanogaster (Oregon) culture has been grown with standard nutrient (SN) in constant incubator conditions since 2014 (25 °C, 60% humidity, 12 h light/dark; [48]). The experimental setup was formed by adding NF materials on the SN (first Group: Control group with only SN, second Group: SN covered with ZrSn, third Group: SN covered with Zr2Sn ratio material, fourth Group: SN covered with 2ZrSn material on top). First instar larvae were obtained after mating by selecting female and male individuals of the same age from the culture. 100 first stage larvae were inoculated to each experimental group under aseptic conditions (total n = 400). First of all, the toxic effects of three materials [49,50] were tried to be determined for toxicity. Insects were followed daily at the same time to calculate patch rate and development time (larvae, pupae, adult; [51]). Male and female individuals were separated under a binocular microscope under cold anesthesia for biochemical analyzes on the third day following mating [52]. Ultrasonic homogenization of the samples (25 male and 25 female individuals for each group) was performed with 250 ml cold buffer ([52]; pH: 7.4). To confirm whether there was a toxic effect, samples were immediately analyzed for TOS (μmol H_2O_2Eq/L) and TAS (mmol Trolox Eq/L) with spectrophotometer (Biochrom Libra) using commercial kits (Baran Medical, Ankara). The oxidative stress index (OSI = TOS/TAS) of the samples was calculated [53].

2.5.1. Antimicrobial effect

Materials (ZrSn, Zr2Sn, 2ZrSn) were first taken to equipment culture (in blood agar and EMB, 24 h). Test substances (ZrSn, Zr2Sn, 2ZrSn) were added to 8 mm diameter wells drilled on Nutrient Agar (NA). Then, *Escherichia coli* (ATCC 35218) and *Staphylococcus aureus* (ATCC 29213) activated in Tryptic Soy Broth were diluted with 0.9% NaCl and inoculated into the samples prepared in NA by cast plate method. Ampicillin disk was used as a positive control. After the petri dishes were incubated at 37 °C for 48 h, the inhibition zones were measured with a caliper (in mm).

2.5.2. Data analysis

Toxicity experiments, antimicrobial activity and biochemical analyzes were performed in triplicate. Data mean and standard deviation of the samples were calculated. In the evaluation of the data, SPSS (version 27) package program was used to determine the variation within the group, One-Way Analysis of Variance (ANOVA) and LSD Test for the significance of the difference between the means. The significance of the
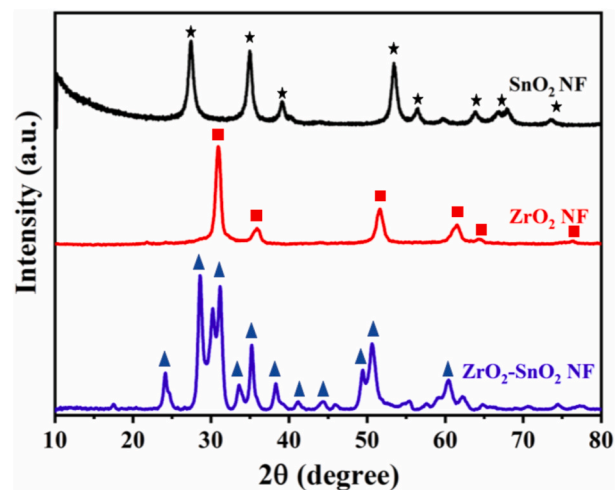

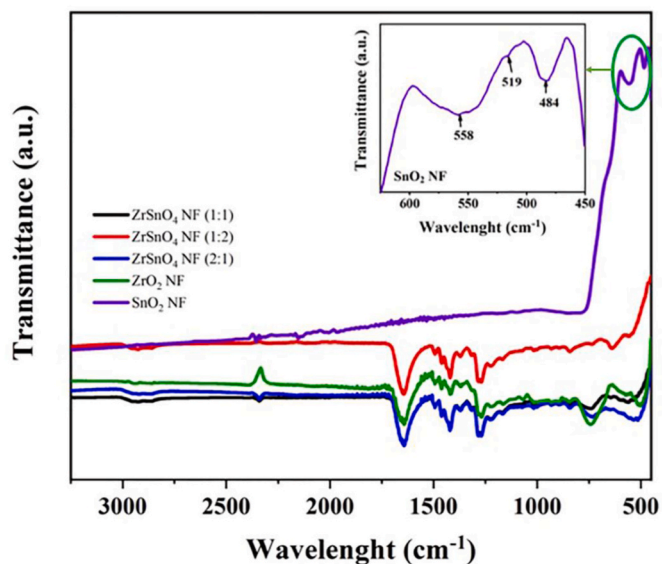**Fig. 3.** XRD patterns of heat treated SnO_2 and ZrO_2 NF and ZrO2–SnO2–ZrSnO4 CNFs.

Fig. 4. FT-IR spectrum of ZrSn, Zr2Sn, 2ZrSn CNFs, and pure ZrO_2, SnO_2 NFs (insets on the top figure presents the magnification of the circled field).

means was assessed within the 0.05 probability level.

3. Results and discussions

3.1. Powder characterization

Crystal structures of heat-treated CNFs for pure form of ZrO_2 and SnO_2 fibers along with ZrSn composition were examined by XRD analysis (Fig. 3). The pattern given in the figure belongs to the NFs sample after heat-treated at 550 °C in air. All the diffraction peaks in this pattern can be indexed to tetragonal structure of SnO_2 and cubic phase of ZrO_2 NF matched up with JCPDS Card No 88–0287 [39,54] and 49–1642 [55, 56], respectively. This shows annealing steps occurred successfully and no extra peak corresponding and any impurity peaks for the crystallization phase of SnO_2 and ZrO_2. In addition, crystallite size of SnO_2 and ZrO_2 NF was calculated with Scherrer equation [39]. By using major peaks, this average calculation resulted in 26 nm and 13 nm for SnO_2 and ZrO_2, respectively. The bottom pattern in this figure quite well matching with orthorhombic phase of $ZrSnO_4$ (JSPCDS Card No
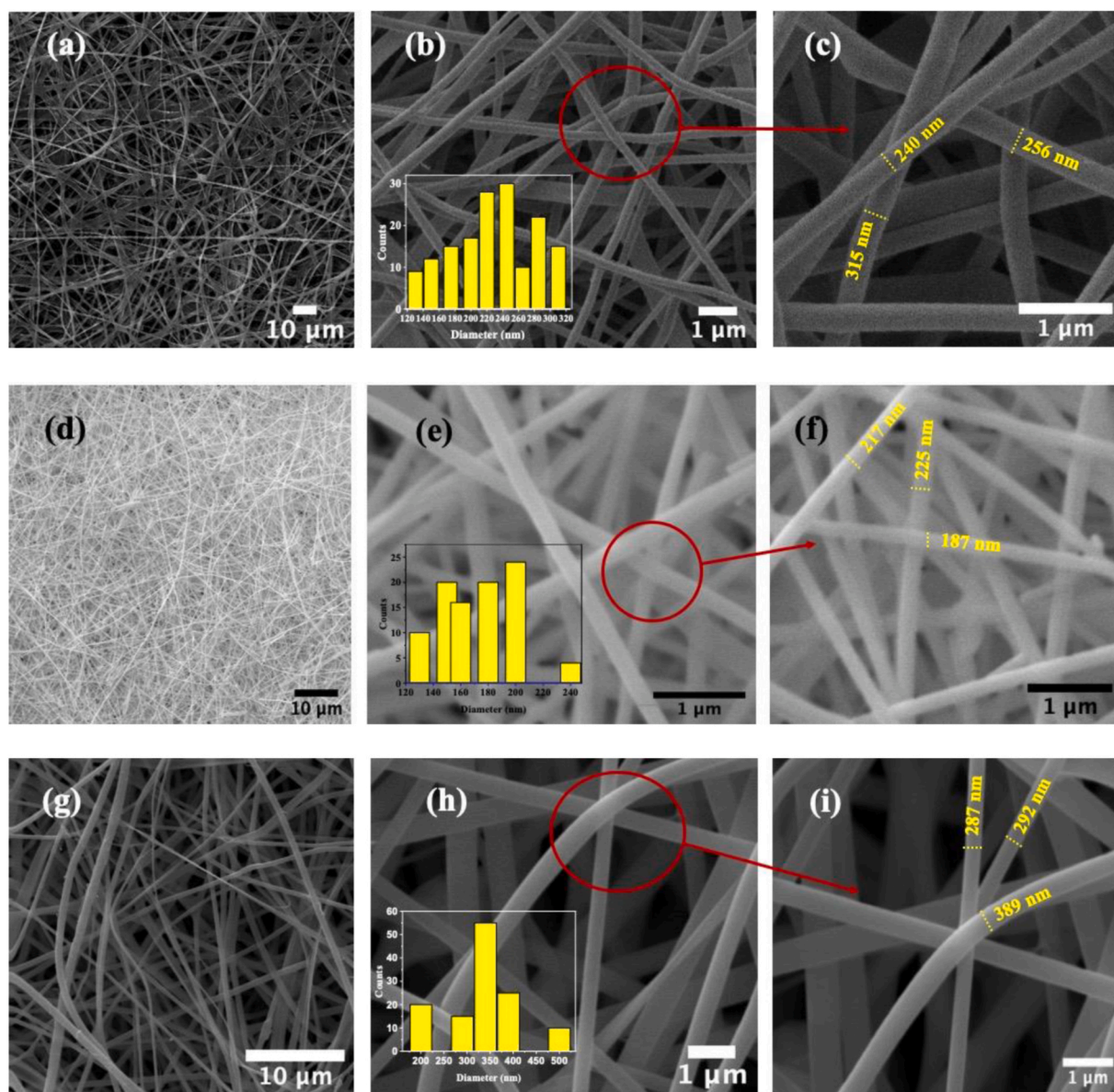
Fig. 5. SEM images of a, d, g) as collected ZrSn, Zr2Sn and 2ZrSn CNFs, respectively and b, c, e, f, h, i) as annealed CNFs in the same order. (insets on the bottom in each middle figures presents the frequency of the calculated diameters of the fibers).

048–0889) [27,29,31]. However, not all the peaks of the collected ZrO_2 and SnO_2 CNFs were transformed into $ZrSnO_4$. Therefore, the ternary system compose of ZrO_2–SnO_2–$ZrSnO_4$ was achieved by this process. The 2ZrSn system revealed ZrO_2 enriched nanocompositions where Zr2Sn nanocomposition contained SnO_2 as a major content.

Fig. 4 shows FT-IR spectra of pure ZrO_2, SnO_2 NFs and composite forms of the ZrO_2–SnO_2–$ZrSnO_4$ CNFs which are ZrSn, Zr2Sn and 2ZrSn NFs. All samples were annealed at 550 °C for the removal of the organic species and formations. After annealing process, the bands become stronger and supporting the formation of the Zr − O− Sn. The characteristic peaks of PVP were located 2949, 1650, 1424, and 1290 cm^{-1} defined to the CH_2 unsymmetrical stretching C = O stretching, CH_2 bending, and C − N stretching vibration bands, respectively [44]. After heat treatment at 550 °C PVP peaks disappeared and pure SnO_2 NF displayed two peaks located at 558, 519 and 484 cm^{-1}. The former peak can be assigned to the Sn − O− Sn and Zr− OH stretching mode of surface-bridging oxygen formed by condensation of adjacent surface oxide groups and the latter peaks associated with stretching vibrations of Sn− O which is confirms the formation of the SnO_2. Besides, the

existence of this peaks occurrence Zr − O− Sn, Zr− O and Sn− O bands which are approving the composition of the composite nanomaterials. Zr− O− C and − OH bands vibrations are 1015 and 1641 cm^{-1}, respectively showed in Fig. 4. Non-bridging − OH groups' vibration peaks at 1415 cm^{-1} [39].

The morphology of the as-collected fibers and heat-treated ZrO_2–SnO_2–$ZrSnO_4$ CNF structures were examined by using SEM in Fig. 5. ZrSn, Zr2Sn and 2ZrSn CNFs have smooth, bead-free and wire-like structures and average diameters before heat-treatment was found 320, 290 and 540 nm, respectively. According to the SEM images in Fig. 5b,e and h, after annealing at 550 °C, the all NFs were still continuous and which indicates that the NFs preserved their uniform structure and average diameters are 230, 185 and 360 nm, respectively.

The frequency of the measured diameters of the NFs in annealed state was shown as an inset in Fig. 5b, e and h. Calcination in air at 550 °C for 5 h resulted in between ∼ 28–36% shrink in the average diameter of the as-collected NFs. Fig. 5c, f and i shows the point of the circled places magnification area for the indicating the fibers diameter. Furthermore, Fig. S1 shows the point EDS analysis taken from the surface of the NFs.
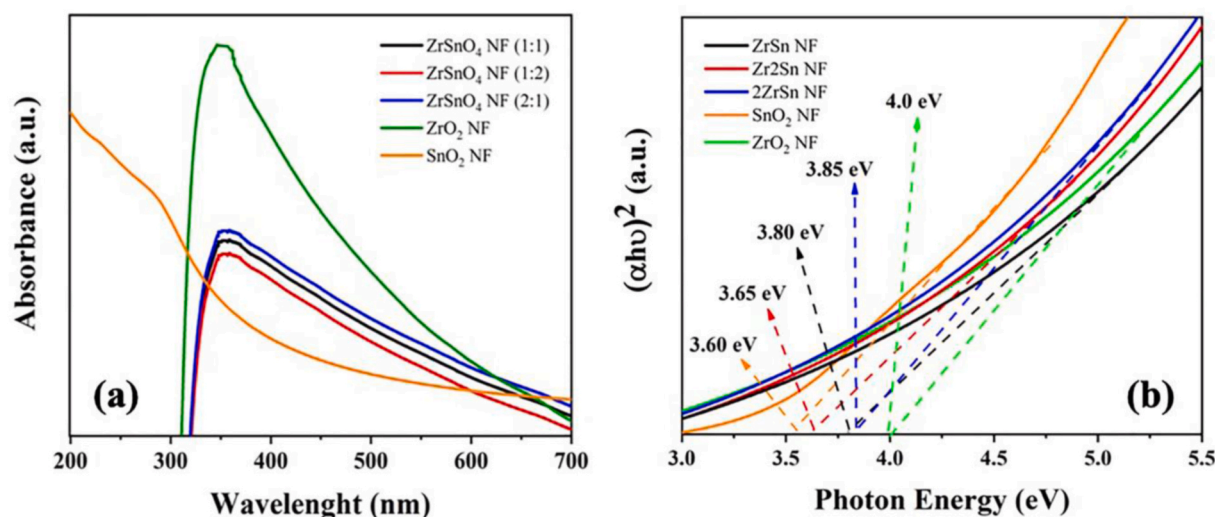
Fig. 6. a) The UV–Vis spectra of ZrSn, Zr2Sn, 2ZrSn and pure ZrO_2 and SnO_2 NFs, (b) plots of $(\alpha h\upsilon)^2$ as a function of photon energy with values of the band gap for pure and various amount of ZrO_2–SnO_2–$ZrSnO_4$ and pure ZrO_2 and SnO_2 NFs.

EDS analysis demonstrated the presence of the Sn wt.% in the composition at the certain ratios designed for the fiber composition.

Examination of bandgap properties for homogeneously structured composite ZrO_2–SnO_2 NFs has been additionally checked for supporting evidence for FS properties research. Fig. 6 shows the absorbance behavior of electrospun ZrO_2–SnO_2–$ZrSnO_4$ CNFs in the wavelength range of 200–700 nm. As illustrated in Fig. 6, NFs displayed absorbance not only in UV but also in the visible region. Pure and composite ZrO_2 NFs were investigated using UV–vis spectrophotometer in the wavelength range between 200 and 700 nm to determine the effect of SnO_2 composition amount on the band gap properties of the NFs. The optical absorption of pure and composite ZrSn, Zr2Sn and 2ZrSn CNFs are given in Fig. 6a. For the comparison with the NFs pure SnO_2 NF's absorbance value is also included in the graph. As seen Fig. 6a, curves of the pure and NFs display absorption bands in the ultraviolet wavelength area but close to the visible-light range.

Compared with the pure NFs (ZrO_2 and SnO_2) the absorption edges of other NF samples have almost similar degrees of blue shift and the absorption is enhanced. Existence of Sn in the composites makes new energy level formed in the band gap, so the peaks shifted the range of 322 nm–340 nm. In addition, the absorption edge is resulted at 310 and 344 nm for pure ZrO_2 and SnO_2 NFs and 326.3, 339.7 and 322.1 nm for composite ZrSn, Zr2Sn, 2ZrSn NFs, respectively. According to the information in Fig. 6a, it was drawn the relationship between $(\alpha h\upsilon)^n$ and $h\upsilon$ and calculate the extrapolated intercept relative to E_g which is Tauc formulation. The band gap of the NFs was found using Tauc equation [54]:

$$(\alpha h\upsilon)^n = A\left(h\upsilon - E_g\right) \tag{1}$$

In this equation, where α is the absorption coefficient and $h\upsilon$ is the photon enrgy. The E_g values of the CNFs results correspond to band gaps 4.0, 3.60, 3.80, 3.65 and 3.85 eV in the same order (Fig. 6b).

The increase of Sn dopant has resulted in the interference-free region of the Zr − Sn catalyst being shifted from 4.0 eV to 3.60 eV. This behavior suggests that the band gap of the catalyst has decreased. The increase in the volume ratio of the Zr cation or the spin-exchange interaction between a Zr ion and an electron-carrying electron may have caused the band gap to decrease [54,57]. The first interaction decreases the bottom of the valence band, while the second interaction widens the top of the valence band. Therefore narrowing the band gap. The formation of Zr defect states due to the trapping of Zr atoms in the forbidden band has been observed [58]. As the Zr doping molecules increases, the density of these defect states increases, which results

increasing band gap or red shift decrease.

In order to demonstrate the effect of Zr defect states on the fiber size, Anitha et al. (2016) introduce a concept called the "*average crystallite size*". As the fiber size of the sample decreases, more and more disorder will be introduced into the sample. This phenomenon is referred to as *crystal disorder*. Since the Zr − Sn NF has a smaller radius than the Zr ions, more disorder will be introduced into the particles as the Zr content increases. The results of this study show that the reduction of the band gap energy by doping with SnO_2 can lead to the substitution of Zr^{+4} with the Sn ions enable the formation of Zr^{3+} ions. This phenomenon can also distort the lattice structure and increase the oxygen vacancy concentration in the solution [44,54].

3.2. Flash sintering ZrO_2–SnO_2–$ZrSnO_4$ CNFs

An electric field of 420 V/mm was imposed on all three ZrO_2–SnO_2–$ZrSnO_4$ CNF samples in the parallel plate capacitor geometry. The current density cut-off was determined as 3.77 mA/mm^2, which is the limit the power supply switches from voltage control to current control automatically. In other words, the voltage was kept constant to ensure the cut-off current density was not exceeded. The specimen was the heated with 20 °C/min heating rate, and the current-voltage data was recorded as a function of time as depicted in Fig. 7. Three stages in FS were identified: (i) the incubation stage is the period on that very small current draw is observed with monolithic increase (ii) the transition stage where the current rises rapidly to its maximum cut-off value at which point the power source switches from voltage to current control; and (iii) the steady-state both the current and voltage are kept constant [19,20].

Initially, no current draw for ZrSn sample until $T_f = 843$ °C (furnace temperature) was detected, which suggests that ZrSn sample shows insulator behavior for 25 °C < T_f < 662 °C under 420 V/mm. In other words, ZrSn sample is a powder compact with green density, where 420 V/mm applied electric field is not enough to lead a current draw through sample due to lack of proper particle-to-particle contacts and low conductivity up to 843 °C. A current leakage of 0.05 mA/mm^2 was observed when T_f is increased 843 °C which the beginning of the incubation stage. Further increase in temperature up to 861 °C leads an increment in the current draw to 1.0 mA/mm^2 in less than 60 s. Thereafter, transition state is initiated for the specimen which exhibits a rapid increase in the current draw, climbing up to the current cut-off limit (3.77 mA/mm^2) at 864 °C in 5 s. At this point the specimen draw max power absorption of 1.58 W/mm^3. The power source switched from voltage control to
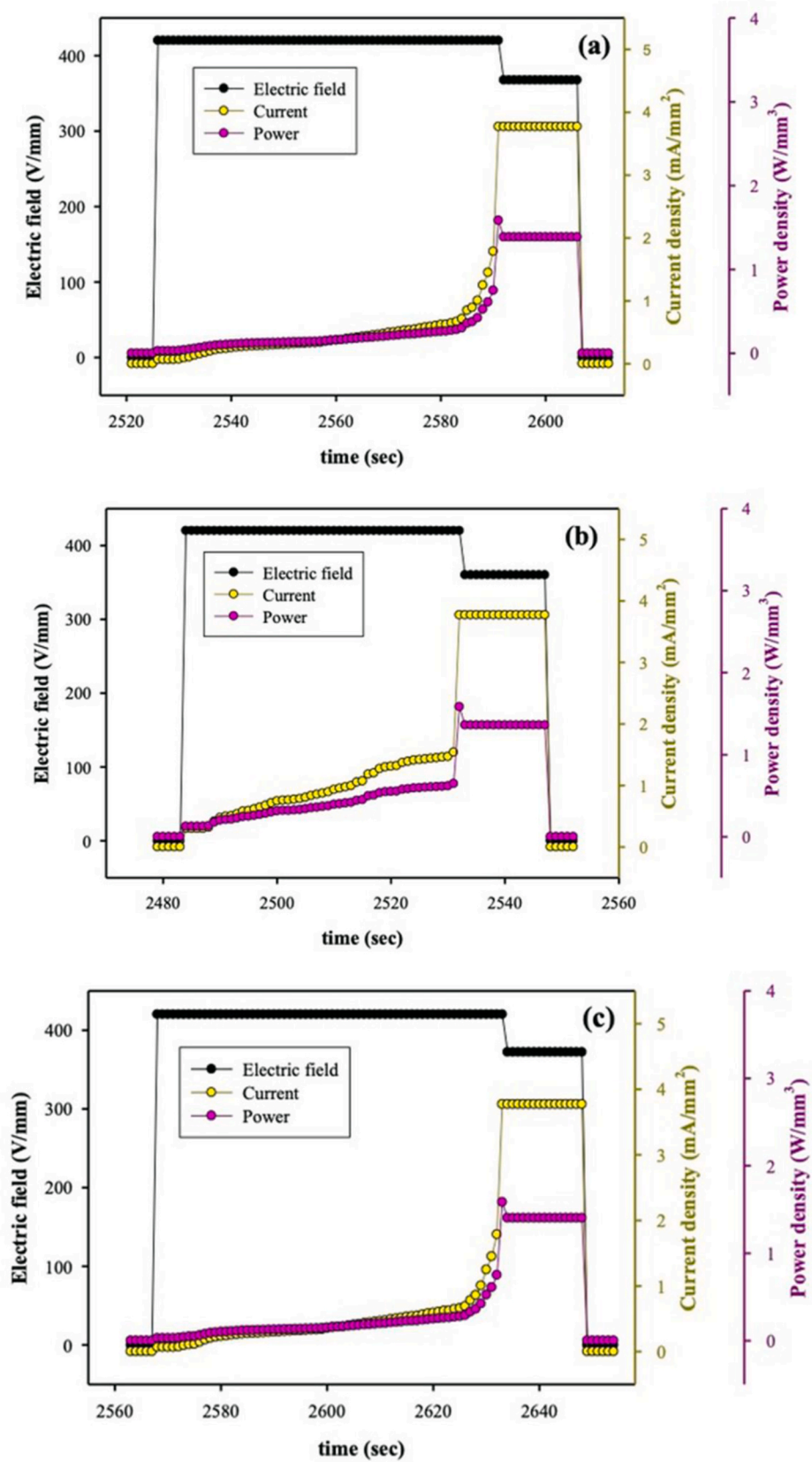
Fig. 7. Current and power behavior as a function of time under 420 V/mm electric field and with 20 °C/min heating rate during FS of a) ZrSn, b) Zr2Sn, c) 2ZrSn. The current cut-off was determined as 3.77 mA/mm^2.
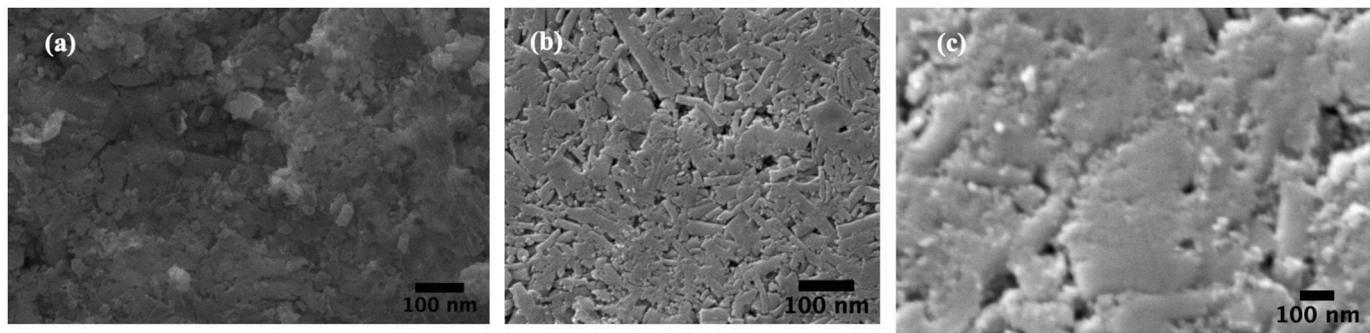
Fig. 8. Microstructure assessment of a) ZrSn, b) Zr2Sn, c) 2ZrSn nanocompositions.

current control for preventing the excessive joule heating. Hence, the power source decreased the electric field down to 365 V/mm to stabilize current limit at 3.77 mA/mm^2 which is defined as the steady state stage for the FS. Further power absorption during the steady state would have caused to excessive Joule heating which would cause abnormal grain growth. Therefore, power was shut down within 15 s once the current density stabilized at 3.77 mA/mm^2 after the point $T_f = 864$ °C. More-over, we consider the 15 s spanning during steady state stage as part of the FS process for ZrO_2 - SnO_2 in conjunction with fixed electrical con-ductivity for a highly dense specimen. We conjecture that the space charge rearranges to its equilibrium configuration within 15 s, following the completion of grain boundary formation at 864 °C under the boundary conditions of this study.

In case of other two composites (Zr2Sn and 2ZrSn) different flash event was observed in terms of three stages of FS. Current leakage temperature for Zr2Sn and 2ZrSn samples was measured at 829 °C and 857 °C which is directly related materials conductivity behavior along with band structure in compositions. ZrO_2 materials system shows higher band gap value comparing with SnO_2, so higher value of band gap leads the current draw at higher temperatures. Different conduc-tivity type along with band gap structure the FS temperature are differentiate as reported many studies [3,4,6,7,9–17,20]. Higher content of ZrO_2 in 2ZrSn composites exhibit current draw at higher temperature where increasing SnO_2 content in Zr2Sn composites leads current leakage at lower temperatures. A closer look to incubation time for the Zr2Sn and 2ZrSn composites, the composition content also effect incu-bation time as well. Zr2Sn composites showed shorter incubation time comparing with other two systems where the higher incubation times were observed for 2ZrSn materials system. Overall, the conductivity and band structure of materials system also determined the incubation time. The rest of the experimental stages for Zr2Sn and 2ZrSn composites was proceed as the ZrSn materials system and no singularities was observed.

As presented in the foregoing, ZrO_2 - SnO_2 composites reached the preset maximum current limit (3.77 mA/mm^2) at different temperature. To understand FS mechanism the amount of power absorption by the ZrO_2 - SnO_2 materials systems is crucial. Joule heating is the one extensively studied to explain such mechanism. It is hypothesized that the local temperature at particle-particle contacts diverges to tempera-tures in the vicinity of the melting point. Consequently, very high diffusion rate is matter at high thermal activation. In this study, less Joule heating was expected because of the relatively low cut-off current density and the short duration of the precipitous densification which was complete in less than 80 s. Despite the foregoing reasoning, we have computed for all samples' temperature using the blackbody model given by Ref. [59].

$$T^{\otimes} = T_f \left[1 + \frac{W}{\Xi T_f^4} \left(\frac{\Omega}{\Lambda} \right) \right]^{\frac{1}{4}} \quad (2)$$

where $T^{\otimes}$ and T_f are designated for specimen and furnace temperature, respectively. W is the power absorbed by the specimen, Ξ is the

blackbody radiation constant (5.67 × 10^{-8} W/(m^{2}K^4)), and (Ω/Λ) is the surface-to-volume ratio of the specimen.

The result suggested a specimen temperature within 10% of the furnace temperature, which has limited effect for the ultra-rapid densification of ZrO_2–SnO_2–$ZrSnO_4$ at 864 °C. Hence, Joule heating is not the only governing mechanism in FS of ZrO_2 - SnO_2. Most impor-tantly, FS which allow us acquire highly dense sample, was accom-plished at $T_f = 864$ °C in less than 80 s in this study, which is reasonably convenient to conventional sintering of $ZrO_2 - SnO_2$ materials system accomplished in 1 h h at 1200 °C [44,54]. Parallel plate capacitor ge-ometry experimental setup provide uniform electric field thorough out sample which the one the factor for sintering at low sintering time and temperature with a reasonable density value.

Microstructure assessment for the flash sintered of ZrO_2–SnO_2–Zr-SnO_4 (see Fig. 8) suggested lack of local melting on grain boundaries which eliminates the hypothesis of excessive Joule heating during the FS of ZrO_2–SnO_2–$ZrSnO_4$ materials system. Moreover, fibers transformed into flat and proper grain boundaries with limited grain growth which is the typical short range mass transport during transient state FS. The formation of the pores illustrated in Fig. 8, which are aroused on the vicinity of grain boundaries, could be related with following reasons: (i) Lack of particle-to-particle contact for the as-pressed sample before FS, (ii) formation of vacancy clustering triggered applied electric field and current flow during FS. The origin of the residual porosity formation is not main focus for this study. Even though, the diffusion flux in this FS study is not sufficient to eliminate whole surface porosity, this micro-structure formation of end product is suitable for biochemical activity experiments. FS allows us have highly dense sample at low temperature in short time period, which limits the grain growth, so the end product of nanocompositions reveals nanostructured surface morphology and en-ergy which eventually huge effect on the biochemical surface properties.

3.3. Toxicity, survival and developmental tests on ZrO_2–SnO_2–$ZrSnO_4$ CNFs

As a result of the toxicity test performed on the larva of the insect, it was determined that all three materials were non-toxic. This result co-incides with the life-development experiments of the insect (Fig. 9a and b). When the control group and other groups were compared, it was observed that the survival rates of larvae, pupae and adults were similar except for the fourth group (95–98%). Although the fourth group decreased the survival rate statistically, it was determined that it was not toxic (85%). The third and fourth groups extended the development time (only 1 day) of the insect somewhat, but except for the third group, the sex ratio (Fig. 9c) did not change much (female/male; 50/50%). The third group sex turned in favor of the female ($F_{15} = 3.86$, $p = 0.02$).

Generally, Nanoparticles which cause toxicity, reduce the survival rate and hatching along with weight loss and growth retardation [34, 62]. Among the nanomaterials found to be non-toxic in *D. melanogaster*, 2ZrSn reduced the survival rate to 85%; While the development time of the insect was around 9 days from the larval stage, Zr2Sn and 2ZrSn

(a)

(b)
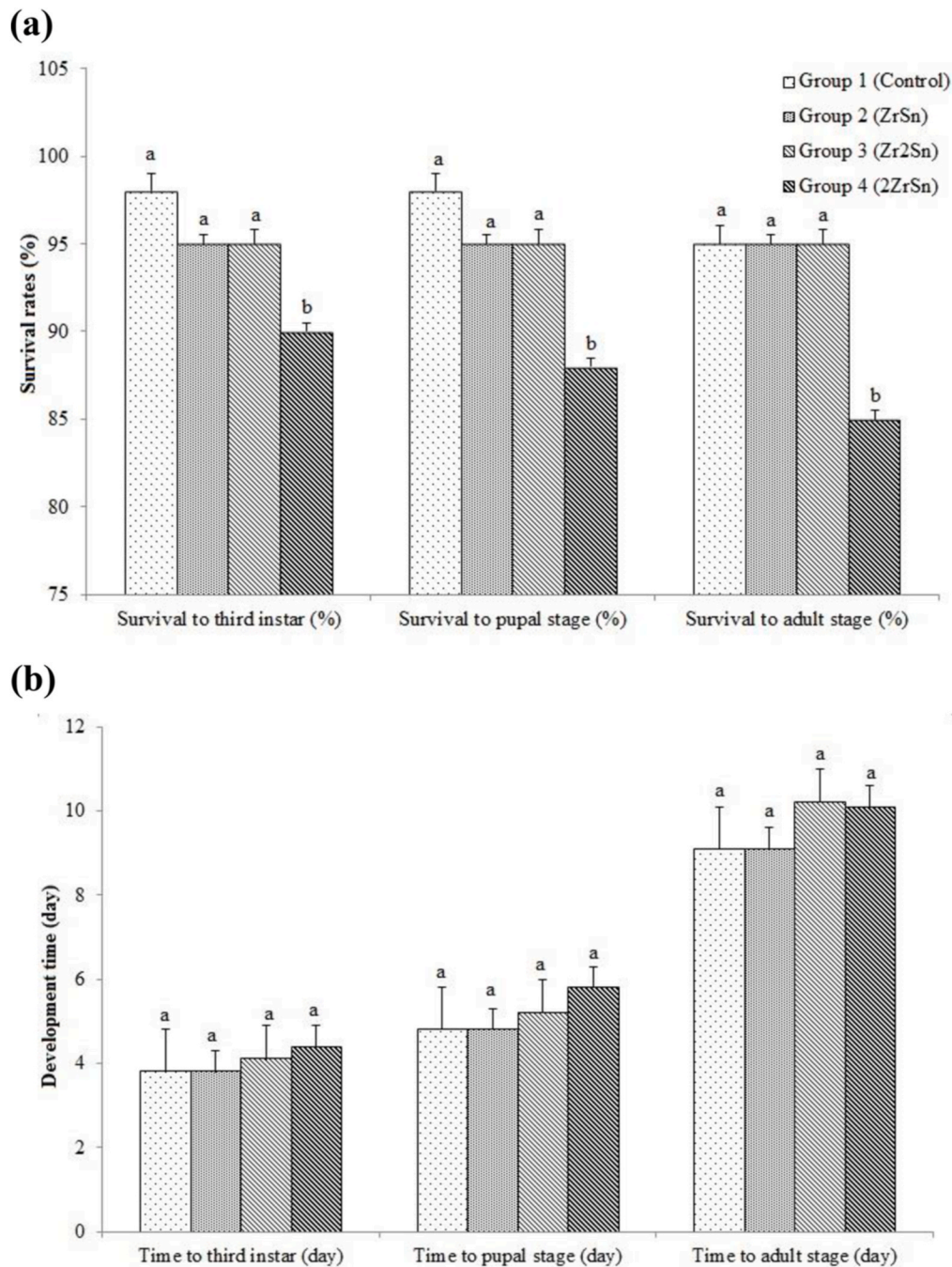
Fig. 9. Insect a) survival rate, b) development time and c) sex ratio table from larval stage to adult (Different letters given between groups belonging to the same developmental period indicate statistical differences; $p < 0.05$).

caused a one-day prolongation in development time (10.2 ± 0.1 day; Fig. 9b; $p < 0.05$). Only in the Zr2Sn group, the gender shifted in favor of the female individual ($55/45 \pm 0.4\%$; Fig. 9b), while the genders were equal in other groups. In parallel with our study, several material system such as zinc oxide nanoparticles show non-toxic behavior. Furthermore, titanium oxide nanoparticles do not affect larval survival while non-toxic doses of polymeric nanoparticles do not affect insect viability. Besides zirconia nanoparticles cause developmental delay as verifying our results [34].

3.3.1. Antimicrobial effect

There was no reproduction according to the culture of the material/equipment. As a result of antimicrobial activity tests related to the produced nanomaterial (ZrSn, Zr2Sn, 2ZrSn), the antimicrobial activity was determined against *S. aureus* and *E. coli* (Fig. 10). Furthermore, it was determined that all material systems were more effective against *E. coli* where Zr2Sn was stronger antibacterially (5.3 ± 0.2 mm; 9.2 mm for Ampicillin).

According to the antimicrobial effect studies, although the material system, produced in this study, have good antimicrobial activity, stronger effect of Zr2Sn has been determined that due to existence of excessive amount of SnO_2 (Fig. 10). This effect is thought to enable ZrO_2–SnO_2 nanocompositions to be more effective in *E. coli*, since the cell wall of *S. aureus* has a thick peptidoglycan layer. Our results show
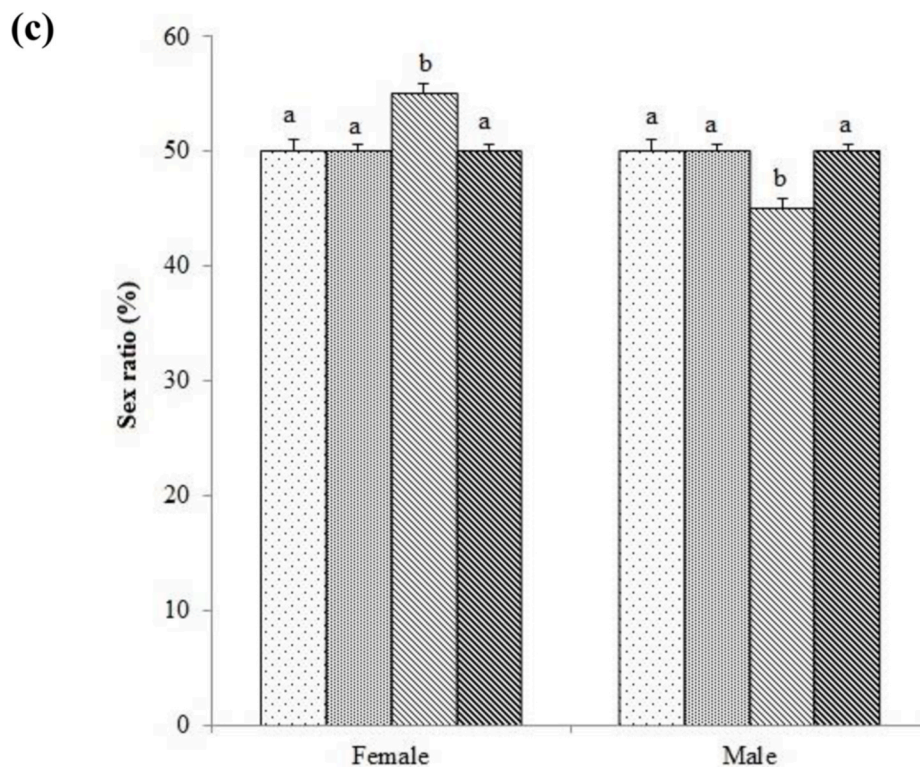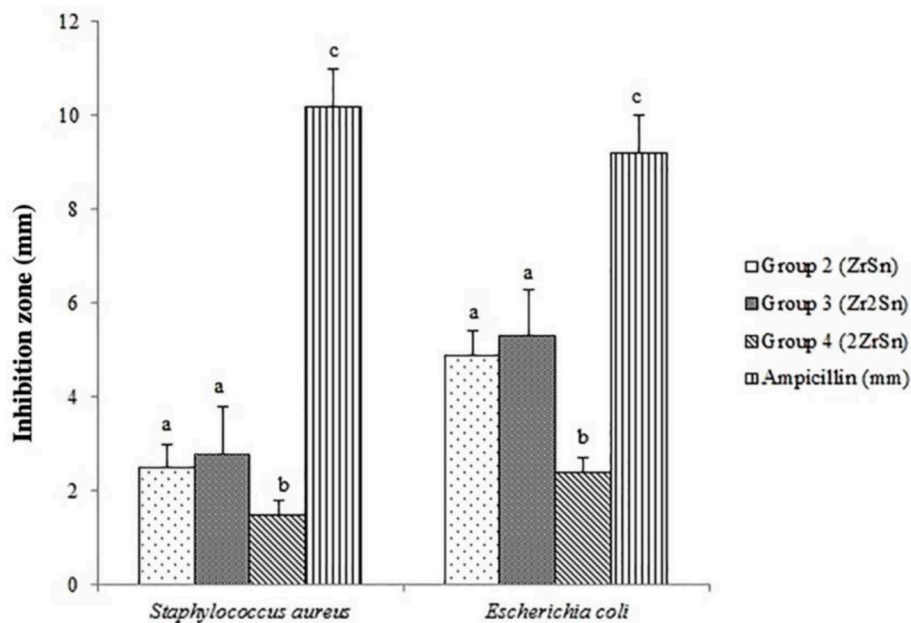
(c)

Fig. 9. (*continued*).

Fig. 10. Zone of inhibition (ZOI) of ZrSn, Zr2Sn, 2ZrSn on *E.coli* and *S. aureus*.

parallelism with antimicrobial studies conducted with ZnO_2 and SnO_2 [2,60,61].

3.3.2. Biochemical analysis

Although TAS activities were similar among females (approximately 3.01 ± 0.02 mmol Trolox Equiv/L), small fluctuations in TOS were detected. According to the OSI results of the females, there was no statistical difference within the group (0.07–0.09 μmol H_2O_2 Equiv/L). While TAS and TOS were decreased in male individuals, OSI results were similar to female individuals (Fig. 11; $p < 0.05$).

Some nanoparticles, such as cerium oxide, have medical therapeutic potential [38]. According to our OSI results, stress for nanomaterial contact could not be determined between the sexes (both males and females) (Fig. 11). Iron oxide nanoparticles with low cytotoxicity reduce the level of ROS in *Drosophila* [34,63]. Cerium oxide nanoparticles are known to reduce oxidative stress [64]. Based on similar studies, it was determined that the nanomaterial used did not increase or decrease oxidative stress.
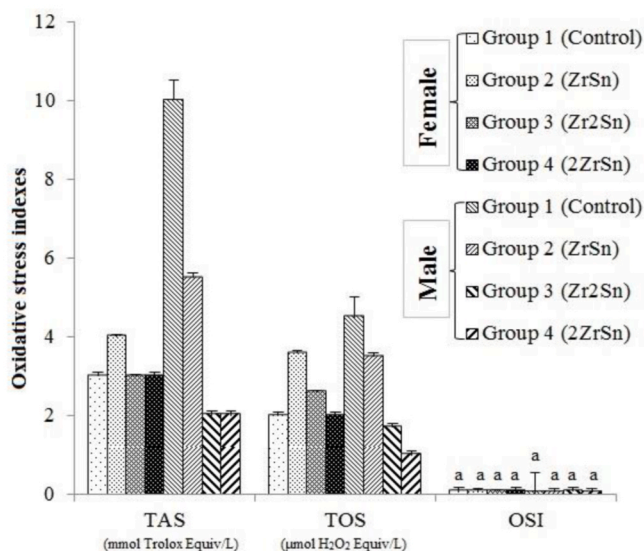
Fig. 11. Oxidative stress index of adult female and male individuals grown with nanomaterial (Similar lowercase letters indicate that there were no significant differences between groups; $p < 0.05$).

4. Conclusion

ZrO_2–SnO_2–$ZrSnO_4$ CNFs were produced via mixing three various volumes (ZrO_2–SnO_2 – ZrSn; 1/1, ZrO_2–$2SnO2$ –Zr2Sn; 1/2, $2ZrO_2$–SnO_2 – 2ZrSn; 2/1) by electrospinning technique. The microstructure and morphological properties of each annealed CNF samples were characterized with XRD, FT-IR, SEM, UV analysis and results showed the ternary system of ZrO_2–SnO_2–$ZrSnO_4$. Besides, as the volume of SnO_2 increases in the CNFs increases, the diameters of the fibers tend to decrease along with decrement in the band gap. The FS experiments were carried out under thermal (844–878 °C) and electric field (420 V/mm) with 3.77 mA/mm^2 current cutoff limit. The max power absorption of 1.58 W/mm^3 let to highly dense nanocompositions in less than 80secs. Due to the low sintering temperature and time, nanostructured surface morphology were aroused which eventually determine the surface biochemical properties of nanocompositions.

Regarding biochemical approach, *D. melanogaster* food was covered with nanocomposition systems (ZrSn, Zr2Sn and 2ZrSn in addition to the control food). The toxicity of the nanomaterial in the insect, survival rate (%), development time (days) were analyzed. In order to support the results, biochemical analyzes (total oxidative level-TOS, total antioxidant level-TAS and oxidative stress index-OSI) were performed in adults. In addition, antimicrobial activity was evaluated with *E. coli* and *S. aureus*. It was determined that the nanomaterials used had an antimicrobial effect and did not have a toxic effect on the insect. It was found that it did not affect the survival rate of the insect in all groups. Even though there was a one-day difference in development times, it did not cause a statistical change in the OSIs of female and male individuals. We believe that the synthesized nanomaterials can be used as a valid candidate in the healthcare system, such as the production of dental implants, due to its antimicrobial effect and non-toxicity in the model organism.

Ethics committee permission

Ethics committee approval is not required for this study.

Financial Support

The authors gratefully acknowledge the financial support provided

CRediT authorship contribution statement

Zeynep Çetinkaya: Writing – original draft, Data curation, Formal analysis, Investigation, Conceptualization, Methodology, Visualization. **Eda Güneş:** Conceptualization, Methodology, Writing – review & editing. **İlyas Şavkliyildiz:** Conceptualization, Methodology, Writing – review & editing.

Declaration of competing interest

The authors declare the following financial interests/personal relationships which may be considered as potential competing interests: Zeynep Cetinkaya reports financial support was provided by Konya Technical University. Zeynep Cetinkaya reports a relationship with Konya Technical University that includes: funding grants. Corresponding author and co-author (Zeynep Çetinkaya and İlyas Şavkliyildiz, respectively) employed by Konya Technical University. Eda Güneş employed by Necmettin Erbakan University.

Data availability

No data was used for the research described in the article.

Appendix A. Supplementary data

Supplementary data to this article can be found online at https://doi.org/10.1016/j.matchemphys.2022.126900.

References

[1] K. Kaviyarasu, L. Kotsedi, A. Simo, X. Fuku, G.T. Mola, J. Kennedy, M. Maaza, Appl. Surf. Sci. 421 (2017) 234–239.
[2] A.B. Ali Baig, V. Rathinam, J. Palaninathan, Appl. Water Sci. 10 (2020) 1–13.
[3] R. Coble, Sintering Crystalline Solids. I. Intermediate and Final State Diffusion Models, Sintering Key Papers, Springer, 1990, pp. 55–67.
[4] R. Coble, Sintering Crystalline Solids. II. Experimental Test of Diffusion Models in Powder Compacts, Sintering Key Papers, Springer, 1990, pp. 69–83.
[5] M. Bocanegra-Bernal, J. Mater. Sci. 39 (2004) 6399–6420.
[6] M. Mitomo, S. Uenosono, J. Mater. Sci. 26 (1991) 3940–3944.
[7] V. Mamedov, Powder Metall. 45 (2002) 322–328.
[8] E. Akdoğan, İ. Şavklıyıldız, H. Biçer, W. Paxton, F. Toksoy, Z. Zhong, T. Tsakalakos, J. Appl. Phys. 113 (2013), 233503.
[9] M. Cologna, B. Rashkova, R. Raj, J. Am. Ceram. Soc. 93 (2010) 3556–3559.
[10] P. Dahl, I. Kaus, Z. Zhao, M. Johnsson, M. Nygren, K. Wiik, T. Grande, M.-A. Einarsrud, Ceram. Int. 33 (2007) 1603–1610.
[11] J.S. Francis, R. Raj, J. Am. Ceram. Soc. 95 (2012) 138–146.
[12] J.S. Francis, R. Raj, J. Am. Ceram. Soc. 96 (2013) 2754–2758.
[13] M. Cologna, J.S. Francis, R. Raj, J. Eur. Ceram. Soc. 31 (2011) 2827–2837.
[14] X. Hao, Y. Liu, Z. Wang, J. Qiao, K. Sun, J. Power Sources 210 (2012) 86–91.
[15] A. Karakuscu, M. Cologna, D. Yarotski, J. Won, J.S. Francis, R. Raj, B.P. Uberuaga, J. Am. Ceram. Soc. 95 (2012) 2531–2536.
[16] J.-C. M'Peko, J.S. Francis, R. Raj, J. Eur. Ceram. Soc. 34 (2014) 3655–3660.
[17] A.L. Prette, M. Cologna, V. Sglavo, R. Raj, J. Power Sources 196 (2011) 2061–2065.
[18] M. Yu, S. Grasso, R. Mckinnon, T. Saunders, M.J. Reece, Adv. Appl. Ceram. 116 (2017) 24–60.
[19] E. Bichaud, J. Chaix, C. Carry, M. Kleitz, M. Steil, J. Eur. Ceram. Soc. 35 (2015) 2587–2592.
[20] K. Vikrant, H. Wang, A. Jana, H. Wang, R.E. García, npj Comput. Mater. 6 (2020) 1–8.
[21] N.-W. Lee, K.R. Yoon, J.-Y. Lee, Y. Park, S.-J. Pyo, G.-Y. Kim, D.-H. Ha, W.-H. Ryu, ACS Appl. Energy Mater. 2 (2019) 3513–3522.
[22] M. Abd-Elwahed, A. Ibrahim, M. Reda, J. Mater. Res. Technol. 9 (2020) 8528–8534.
[23] m. El-wazery, Int. J. Eng. 26 (2013) 375–382.
[24] E. Akdoğan, İ. Şavklıyıldız, B. Berke, Z. Zhong, L. Wang, M. Vaughan, T. Tsakalakos, Appl. Phys. Lett. 99 (2011), 141915.
[25] E. Akdoğan, İ. Şavklıyıldız, B. Berke, Z. Zhong, L. Wang, D. Weidner, M. Croft, T. Tsakalakos, J. Appl. Phys 111 (2012) 053506.
[26] İ. Şavklıyıldız, E. Akdoğan, Z. Zhong, L. Wang, D. Weidner, M. Vaughan, M. Croft, T. Tsakalakos, J. Appl. Phys. 113 (2013), 203520.
[27] V.S. Anitha, S.S. Lekshmy, K. Joy, Mater. Today Proc. 2 (2015) 1026–1030.

[28] S. Surbhi, S. Kumar, Studies on Structural Parameters of ZrO 2–SnO 2 Binary System, Physics of Semiconductor Devices, Springer, 2014, pp. 717–719.
[29] V. Anitha, S.S. Lekshmy, K. Joy, J. Alloys Compd. 675 (2016) 331–340.
[30] J. Kim, S. Kim, D. Kim, R. Ott, H. Kim, M. Lee, AIP Adv. 5 (2015), 077132.
[31] T. Athar, S.K. Vishwakarma, A. Bardia, R. Alabass, A. Alqarlosy, A.A. Khan, Appl. Nanosci. 6 (2016) 767–777.
[32] S.M. Ibrahim, Renew. Energy 173 (2021) 151–163.
[33] H. Kumar, K. Bhardwaj, E. Nepovimova, K. Kuča, D. Singh Dhanjal, S. Bhardwaj, S. K. Bhatia, R. Verma, D. Kumar, Nanomaterials 10 (2020) 1334.
[34] M. Mishra, M. Panda, Free Radic. Res. 55 (2021) 919–935.
[35] W. Wu, Z. Wu, T. Yu, C. Jiang, W.-S. Kim, Sci. Technol. Adv. Mater. 16 (2) (2015) 1–43.
[36] G. Libralato, E. Galdiero, A. Falanga, R. Carotenuto, E. De Alteriis, M. Guida, Molecules 22 (2017) 1439.
[37] B. Tunçsoy, J. Anatolian Environ. Anim. Sci. 6 (2021) 278–284.
[38] V. Sundararajan, G.D. Venkatasubbu, S. Sheik Mohideen, 3 Biotech 11 (2021) 1–11.
[39] S. Dursun, I.C. Kaya, V. Kalem, H. Akyildiz, Dalton Trans. 47 (2018) 14662–14678.
[40] Z. Çetinkaya, V. Kalem, J. Dispersion Sci. Technol. 43 (7) (2022) 1079–1088.
[41] H. Biçer, E.K. Akdoğan, İ. Şavklıyıldız, C. Haines, Z. Zhong, T. Tsakalakos, J. Mater. Res. 35 (2020) 90–97.
[42] İ. Şavkliyildiz, A. Demir, El-Cezeri J. Sci. Eng. 8 (2) (2021) 793–799.
[43] İ. Şavklıyıldız, Ç. Okur, E.K. Akdoğan, J. Am. Ceram. Soc. 105 (2022) 469–480.
[44] V. Anitha, S.S. Lekshmy, K. Joy, J. Mater. Sci. Mater. Electron. 24 (2013) 4340–4345.
[45] Z. Çetinkaya, Gazi Üniversitesi Mühendislik Mimarlık Fakültesi Dergisi 37 (2022) 137–144.
[46] H. Bicer, B. Beyoglu, T.E. Ozdemir, J. Okasinski, T. Tsakalakos, Ceram. Int. 45 (2019) 7614–7618.
[47] H. Biçer, A. Degnah, E. Salur, İ. Şavklıyıldız, T. Tsakalakos, E.K. Akdoğan, Mater. Today Commun. 33 (2022), 104272.
[48] E. Güneş, E. Büyükgüzel, Turkish J. Entomol. 41 (2017) 3–15.
[49] H. Uysal, S. Semerdöken, Kafkas Üniversitesi Fen Bilimleri Enstitüsü Dergisi 4 (2011) 71–87.
[50] D. Finney, Methods Inf. Med. 10 (1971) 237–245.
[51] E. Güneş, D.A. Danacıoğlu, Anim. Biol. Leiden 68 (2018) 367–385.
[52] E. Güneş, Food Chem. Toxicol. 148 (2021), 111935.
[53] E. Özgün, G.S. Özgün, S. Eskiocak, Ö. Yalçın, S.S. Gökmen, Turkish Journal of Biochemistry/Turk Biyokimya Dergisi 38 (2013).
[54] S. Song, J. Wei, X. He, G. Yan, M. Jiao, W. Zeng, F. Dai, M. Shi, RSC Adv. 11 (2021) 35361–35374.
[55] F. Shi, Y. Li, H. Wang, Q. Zhang, Prog. Nat. Sci.: Mater. Int. 22 (2012) 15–20.
[56] V.S. Reddy Channu, R.R. Kalluru, M. Schlesinger, M. Mehring, R. Holze, Colloids Surf. A Physicochem. Eng. Asp. 386 (2011) 151–157.
[57] V. Mote, J. Dargad, B. Dole, Nanosci. Nanoeng. 1 (2013) 116–122.
[58] V. Sokolov, A. Druzhinin, N. Gruzdev, A. Dejneka, O. Churpita, Z. Hubicka, L. Jastrabik, V. Trepakov, Phys. Rev. B 81 (2010), 153104.
[59] R. Raj, J. Am. Ceram. Soc. 99 (2016) 3226–3232.
[60] N. Tabassum, D. Kumar, D. Verma, R.A. Bohara, M. Singh, Mater. Today Commun. 26 (2021), 102156.
[61] E.B. Tibayan Jr., M.A. Muflikhun, V. Kumar, C. Fisher, C.V. Al Rey, G.N.C. Santos, Ain Shams Eng. J. 11 (2020) 767–776.
[62] S.A. Pappus, M. Mishra, Cell. mol. toxicol. nanopart. (2018) 311–322.
[63] Y. Zhang, Z. Wang, X. Li, L. Wang, M. Yin, L. Wang, N. Chen, C. Fan, H. Song, Adv. Mater. 28 (2016) 1387–1393.
[64] A. Sarkar, T.S. Mahendran, A. Meenakshisundaram, R.V. Christopher, P. Dan, V. Sundararajan, N. Jana, D. Venkatasubbu, S.S. Mohideen, Chemosphere 284 (2021), 131363.